INSTITUTE OF PHYSICS PUBLISHING JOURNAL OF OPTICS A: PURE AND APPLIED OPTICS
J. Opt. A: Pure Appl. Opt. **4** (2002) 408–418 PII: S1464-4258(02)32974-X

Different possibilities for water vapour measurements by lidar in daytime at ENEA's observatory in Lampedusa, Italy: a simulation

F Marenco and P Tini Brunozzi[1]

ENEA/CLIM–OSS, S Maria di Galeria, 00060 Roma, Italy

Received 23 January 2002, in final form 25 April 2002
Published 30 May 2002
Online at stacks.iop.org/JOptA/4/408

Abstract
A few of the available options for Raman and differential absorption lidar measurements of the vertical profile of the water vapour mixing ratio in daytime are compared through numerical simulation. In ENEA's project, such an instrument is to be deployed at the island of Lampedusa for measurements in the Planetary Boundary Layer. The numerical model shows good agreement with independent lidar system simulations from the literature. The results show that DIAL yields a definitely better signal-to-noise ratio than Raman lidar. However, the Raman lidar technique is retained because of the system complexity that would arise with DIAL. The 'solar blind' region has been discarded because ranges larger than 1–2 km cannot practically be reached, and a wavelength of 355 nm has been chosen due to the availability of powerful laser sources that can be kept simple to operate. A dual-receiver system has been found to be necessary for viewing the entire 0.1–3 km range interval.

Keywords: Raman lidar, DIAL, water vapour

1. Introduction

Water occurs in the atmosphere in the solid, liquid and vapour states of aggregation, and plays an important role in several meteorological and climatic processes involving the hydrological cycle, latent heat transport, cloud formation, precipitation, aerosol growth, radiative budget and atmospheric chemistry. Water vapour influences the radiation field directly by acting as a greenhouse gas (by absorption in the infrared part of the spectrum); water clouds also influence the radiation budget through the scattering of the incoming visible radiation and the consequent increase in terrestrial albedo. For these reasons, despite being considered a minor constituent due to its small relative abundance, when compared to the well mixed gases (nitrogen, oxygen and argon), water is without any doubt the most important substance present within the atmosphere. The water vapour distribution and fluxes represent important pieces of information for practically all scientific subjects related to the atmosphere.

Profiles of atmospheric quantities, including the water vapour mixing ratio, are obtained daily at several stations through *in situ* measurements with radiosondes. The radiosonde network is essential, as it represents the backbone of the meteorological observational and forecast capacity [1]. Moreover, radiosonde observations are necessary for remote sensing applications, as they represent the standard against which measurements are compared and calibrated. The disadvantage of radiosondes is the limited horizontal and temporal resolution, which are related respectively to the geographical distribution of meteorological stations and to the launch frequency.

Passive radiometer sensors operating in the microwave and infrared regions represent another possibility for water vapour measurements. Most passive sensors, however, have a poor vertical resolution or yield only column integrated quantities. Such sensors can be ground based or installed on satellites. Satellite measurements overcome the limitation in horizontal

[1] Current address: Istituto Statale di Istruzione Classica, Foligno, Italy.

resolution, but are still limited in temporal resolution. It also has to be said that, since satellites view a large region, their measurements are not always directly comparable to local measurements which represent points on the globe.

Atmospheric profiles can also be measured with active sensors, such as lidar (see, e.g., [2–4]). The advantages of the lidar technique reside in the high temporal and vertical resolutions (of the order of minutes and tens of metres, respectively), with the possibility of making continuous measurements with a large repetition rate at a relatively low cost of operation. Like radiosondes, ground-based lidars cannot, however, solve the problem of poor horizontal resolution and they are limited to clear air (cloud-free) conditions. From what has been said above, therefore, it should be clear that observations can be made complete only by integration of the different available types of instruments.

In the main, two different techniques for measurements of minor atmospheric constituents by lidar are known: Raman lidar and differential absorption lidar, DIAL (see, e.g., [2, 5]). The first is based on Raman scattering, a weak inelastic scattering process by molecules, characterized by a scattered frequency which is shifted by a fixed increment, unique for each molecular species, the missing part of the energy being transferred to the internal rovibrational states. Raman lidar measurements of water vapour have been performed at several research institutions [6–14].

The DIAL technique, instead, uses differential extinction at two neighbouring wavelengths to identify the given constituent, where one of the wavelengths is more absorbed than the other by the target substance. Several DIAL systems have been used to successfully measure water vapour concentration; see, for instance, [15–22].

The Climate Observatory located in Lampedusa, Italy (35.5°N, 12.6°E) is operated by the National Agency for New Technology, Energy and Environment of Italy (ENEA). Lampedusa is a small rocky island in the Southern Mediterranean Sea, located ∼100 km off the coast of Tunisia and ∼200 km off the coast of Libya. Several instruments are installed in the observatory and monitor several important atmospheric parameters, such as the concentration of greenhouse gases, total ozone, aerosol load, solar radiation and meteorological parameters [23, 24]. The Agency wishes to install a lidar system in Lampedusa for the measurement of the vertical profile of water vapour mixing ratio in the daytime planetary boundary layer.

Linné *et al* [25] have identified the main types of application of a water vapour lidar, and have indicated the system performance required for each of them. For continuous monitoring as part of climatological studies, the temporal and vertical resolutions are not crucial, while it is important to reach the largest possible vertical range. For the study of boundary layer processes and turbulent transport, instead, it is important to have a temporal resolution of the order of 10–30 s together with a vertical resolution of 75 m. Finally, for radiation budget applications a high accuracy in both the lower and upper troposphere are desired.

Numerical simulation of lidar systems is a useful exercise for comparing the performance obtainable with different solutions (see also, among others, [21, 22, 26, 27]). Several options are possible, using wavelengths in the ultraviolet (UV) and in the near-infrared. The operating wavelength must be chosen according to several parameters, mainly: atmospheric backscattering cross section, atmospheric extinction, sky background intensity, availability of a laser source and simplicity of operation.

The range interval for which a lidar can be operational is limited (a) in the near range by the geometrical form factor function (incomplete overlap between the receiver field-of-view (FOV) and the transmitted beam); and (b) in the far range by the fast decreasing signal-to-noise ratio (SNR). DIAL would seem to be the best option for daytime measurements, since a more favourable signal-to-noise ratio is achievable; the drawback, however, is an increase in system complexity since the water vapour absorption lines are very narrow. In contrast, a Raman lidar can be simpler in design, but the backscattered signal is weak and, for daytime operation, the main limitations reside in atmospheric extinction and sky background level. Despite all of this, powerful Raman lidar systems for water vapour measurements exist (see, for instance, [12, 13]).

This paper compares the Raman and DIAL techniques through numerical simulation and examines a few of the different available options for daytime boundary layer studies. The computations are used to determine the basic characteristics of our future water vapour lidar system. Section 2 recalls the basic equations needed to evaluate the lidar signal and sky background for given system properties and atmospheric profiles, and highlights how system parameters should be chosen for maximizing system performance. Section 3 briefly discusses the importance of accounting for the geometrical form factors when measurements at the near range are considered, and section 4 discusses the assumptions used in the simulations. The simulation results are presented in section 5, where a comparison with previous literature on lidar system modelling is also given. Finally, section 6 contains a discussion of the results and our conclusions.

2. Numerical evaluation of lidar signals

For daytime measurements at a given emitted wavelength λ, the lidar signal $N(R)$ in photon counts, corresponding to the range R, can be calculated by the following formula (see, e.g., [2]):

$$N(R) = q(R)K_L\frac{\beta(R)}{R^2}T(0,R)T'(0,R) + N_0 + N_D \qquad (1)$$

where K_L is the lidar constant which depends on the instrumental parameters, $\beta(R)$ is the atmospheric volume backscattering cross section (or backscattering coefficient), $T(0,R)$ and $T'(0,R)$ are the atmospheric transmissivities for the upward and the downward paths, N_0 is the sky background and N_D represents the detector dark counts. For a DIAL system, $\beta(R)$ is the elastic (Rayleigh + Mie) volume backscattering cross section and $T(0,R) = T'(0,R)$. For a Raman lidar $\beta(R)$ is the Raman volume backscattering cross section and, since a wavelength shift exists between the emitted beam and the received wavelength, $T(0,R) \neq T'(0,R)$.

The lidar constant can be evaluated as follows:

$$K_L = \eta_o\eta_q\frac{\lambda'\,\Delta R\,\Delta t}{hc}AfE_0 \qquad (2)$$

where λ' is the received wavelength, A is the area of the receiver, E_0 is the laser energy per pulse, f is the pulse repetition frequency, η_o and η_q are, respectively, the optical and quantum efficiencies of the receiver, ΔR is the vertical resolution, Δt is the integration time, h is Planck's constant and c is the speed of light.

The factor $q(R)$ in (1) is the geometrical form factor, which takes into account the incomplete overlap between the emitted beam and the receiver field-of-view. For an aligned system $q(R) = 1$ in the far range, $q(R) < 1$ in proximity of the instrument and $q(0) = 0$.

The background term can be evaluated as follows:

$$N_0 = \eta_o \eta_q \frac{\lambda' \Delta R \Delta t}{hc} A f \, W \Delta\lambda' \frac{2\pi}{c} \left(\frac{\theta}{2}\right)^2 \tag{3}$$

where W is the zenith sky spectral radiance, $\Delta\lambda'$ is the receiver bandwidth and θ is the receiver field-of-view. The dark count rate can be estimated as $d = 100\ \mathrm{s}^{-1}$, as in [27], and thus

$$N_D = \frac{2f}{c} d \, \Delta R \, \Delta t. \tag{4}$$

For daytime simulations $N_D \ll N_0$, except for the 'solar blind' case (see later in section 4.1 for a description of the 'solar blind' approach). The dark counts N_D have been included in the simulations, but for simplicity they have been omitted in the following equations, which can be easily extended.

The detector noise can be evaluated according to photon count statistics as $\delta N = \sqrt{N(R)}$. An important parameter for evaluating lidar performance is the signal SNR, which is the ratio of $S(R) = N(R) - N_0$ (the useful part of the signal) to $\delta S = \sqrt{(\delta N)^2 + (\delta N_0)^2}$. For weak signals in daytime conditions $N(R) \simeq N_0$ and $\delta S \simeq \delta N \simeq \sqrt{N_0}$ (by neglecting δN_0); therefore, it is important to maximize the following ratio, which can be considered as a figure-of-merit for system performance at the far range:

$$\frac{K_L}{\sqrt{N_0}} = \frac{E_0}{\theta} \sqrt{\frac{2\eta_o \eta_q \lambda' A f \, \Delta R \, \Delta t}{\pi h W \, \Delta\lambda'}} \tag{5}$$

and thus to maximize laser pulse energy, receiver area and efficiency, and to minimize bandwidth and FOV.

As, in general, δN_0 cannot be neglected, it has to be accounted for by considering how the background is measured and subtracted for each lidar profile. The determination of N_0 can be done by measuring the signal shortly before the laser pulse is emitted, or after the atmospheric signal following the laser pulse has vanished: accordingly $\delta N_0 = \sqrt{N_0}$. This error can, however, be reduced by repeating the measurement of the background x times (i.e. x data points taken at sufficient distance from the laser pulse). Then, one can take N_0 equal to the mean of these points and δN_0 equal to their standard deviation divided by $\sqrt{x}$; the expected value for this error is $\delta N_0 = \sqrt{N_0/x}$, and thus

$$\delta S = \sqrt{N(R) + \frac{N_0}{x}} = \sqrt{S(R) + \left(1 + \frac{1}{x}\right) N_0}. \tag{6}$$

In the simulations described here we have taken $x = 10$.

Raman lidar allows us to determine profiles of the mixing ratio w by taking the ratio of Raman backscatter by water vapour to Raman backscatter by one of the well mixed gases such as nitrogen [11]:

$$w = C \frac{S_{H_2O}}{S_{N_2}} \tag{7}$$

where C is a system-dependent calibration constant. A more general formula, which includes the correction for ozone absorption at short wavelengths, can be found in [9]. In the case of Raman lidar, the interesting SNR is the one calculated on mixing ratio: $\mathrm{SNR} = w/\delta w$. Since nitrogen concentration is much larger than water vapour concentration, S_{N_2} can be larger than $S_{\mathrm{H_2O}}$ by two to three orders of magnitude, and the uncertainty on $S_{\mathrm{H_2O}}$ dominates the global uncertainty on w: therefore $\mathrm{SNR} \simeq S_{\mathrm{H_2O}}/\delta S_{\mathrm{H_2O}}$. However, in our simulations we have taken into account the full error propagation formula (see [27]), taking into account the errors on the nitrogen signal as well. Systematic errors, arising, for instance, from calibration, will not be considered, since only random errors are examined here, but it has to be mentioned that, according to [27], the absolute accuracy on the calibration constant is around 5%.

For DIAL, the equation that allows the retrieving of the water vapour absolute concentration H, expressed in molecules per unit volume, is

$$H = \frac{1}{2(R_2 - R_1)(\sigma_{on} - \sigma_{off})} \ln\left[\frac{S_{off}(R_2) S_{on}(R_1)}{S_{on}(R_2) S_{off}(R_1)}\right] \tag{8}$$

where R_1, R_2 are two neighbouring (but different) ranges, $\sigma_{on}, \sigma_{off}$ (with $\sigma_{on} > \sigma_{off}$) are the water vapour absorption cross sections at each of the emitted wavelengths $\lambda_{on}, \lambda_{off}$, and S_{on}, S_{off} are the background subtracted signals at both wavelengths. When studying the case of DIAL, we shall consider $\mathrm{SNR} = H/\delta H$, where δH is the noise on H that derives from the full error propagation of the photon counting statistical noise δS, as given in [21]. Provided that the water vapour spectroscopic functions and the emitted wavelengths are exactly known, a DIAL system has an intrinsic absolute calibration. Sources of error on this point are extensively treated in [5].

3. Geometrical form factors

Since we aim at measurements in the lower troposphere, it is important to evaluate the geometrical form factor in the near range, where it can be sensibly different than 1. In fact, while the $K_L/\sqrt{N_0}$ ratio should be maximized in order to reach far atmospheric layers, some of the parameters entering this ratio (i.e. A and θ) also have an influence on $q(R)$, and their effect goes in the opposite direction: in order to have a nearby overlap range the best situation is one with a small telescope and a large FOV.

To go into quantitative estimates, we have made geometrical form factor calculations according to [28], using a numerical computation by Vincenzo Santacesaria [29]. In order to have a complete overlap as close as possible to the lidar, a coaxial geometry has been considered. The next two crucial parameters in determining the overlap range are the telescope size and FOV. We have considered four cases, considering two different telescopes (200 mm and 500 mm in diameter) and

Table 1. Characteristics of the four receiver geometries considered, used as inputs for geometrical form factor calculations. The results are given in the form of half and full overlap range. The full results of the geometrical form factor calculations are given in figure 1.

Telescope Field-of-view	Small Large	Small Small	Large Large	Large Small
Beam divergence (mrad)	0.1	0.1	0.1	0.1
Beam diameter (mm)	50	50	50	50
Primary diameter (mm)	200	200	500	500
Secondary diameter (mm)	50	50	120	120
Focal length (mm)	600	600	1250	1250
Diaphragm diameter (mm)	0.6	0.2	1	0.5
Field-of-view (mrad)	1	0.333	0.8	0.4
Half overlap range (m)	150	460	450	910
Full overlap range (m)	280	1080	780	1830

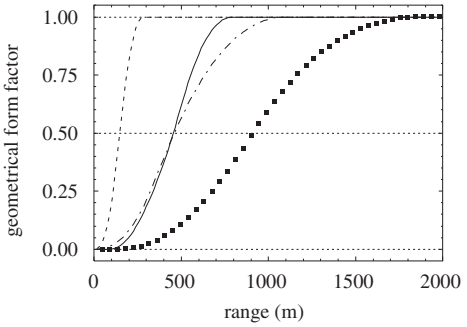

Figure 1. Geometrical form factors for different receivers: small telescope, large FOV (broken curve); small telescope, small FOV (full curve); large telescope, large FOV (chain curve); large telescope, small FOV (full squares). See table 1.

two different FOVs for each telescope (see table 1). In all cases an emitted beam with 0.1 mrad divergence and 50 mm diameter has been assumed (which is normally obtainable from a 0.5 mrad, 10 mm laser beam by using a 5× beam expander).

Figure 1 summarizes the results of the geometrical form factor computations. What we have labelled 'half overlap range' refers to the range where the geometrical form factor is 0.5. Normally, for elastic backscattering lidar measurements one would consider valid only data obtained with a geometrical form factor of 1 (full overlap). However, since for Raman lidar the ratios between signals measured at the same distance at two received wavelengths must be considered, it is admissible to use data obtained at shorter distances. Possible differences in overlap between the channels, arising in the near range, can be corrected for by experimentally determining the ratio between the signals as a function of range before each measurement session, by using Raman nitrogen filters on both channels [11]. This permits us to reach atmospheric layers quite close to the telescope. We have therefore conventionally chosen to consider the 'half overlap range' as the first usable range for water vapour Raman lidar measurements; however, closer ranges are likely to be reached with a real lidar system when the steps indicated above are followed, as documented in [11].

4. Assumptions

Based on equation (1), the measured signal for several options has been simulated. The options that have been considered concern three Raman lidar wavelengths and two DIAL wavelengths (see table 2).

4.1. Raman lidar

Concerning Raman lidar, we are in principle not limited to any transmitted wavelength. The received wavelengths for ν_1 Raman scattering are determined by considering a shift in frequency of 2330.7 cm^{-1} for nitrogen and 3652 cm^{-1} for water vapour [11]. The major problem is that the backscattering cross section is small and the water vapour concentration too, so that the returned signal is about four orders of magnitude less than the combined Mie and Rayleigh signal in an elastic backscattering system. Thus, most available Raman lidar systems are confined to operating at nighttime if a good SNR is required. The Raman backscattering cross section follows a λ^{-4} wavelength dependence, similar to Rayleigh scattering: therefore, short wavelengths are more interesting and the ultraviolet band is most indicated [5]. Working in the UV also allows us to achieve a better detector efficiency than in the visible and near-infrared bands; however, absorption by ozone must be considered, since it dominates the atmospheric radiation field in this part of the spectrum. Ozone absorption prevails below ∼300 nm, and at shorter wavelengths it determines the behaviour of the system with respect to the atmospheric extinction of the signal and sky background.

Two system concepts for Raman lidar are known in the literature, and are related to the choice of wavelength inside or outside the ozone bands. The first approach consists in choosing a wavelength where signal extinction due to ozone absorption is negligible, i.e. $\lambda > 300$ nm. In this case, extinction is due mainly to Rayleigh and Mie scattering, and it remains at acceptable levels. However, for daytime measurements the principal limitation is connected to the sky background, which at these wavelengths can be quite large compared to signal intensity. Nighttime measurements, instead, are easier to carry out due to the absence of solar radiation. Systems following this approach are described, for instance, in [10–13]; [12, 13] describe systems with daytime capability.

In the second approach, known as the 'solar blind' concept, a wavelength is chosen where ozone absorption is strong ($\lambda' < 300$ nm). This drastically reduces the sky background, as solar radiation is strongly attenuated by the ozone layer, so that both day- and nighttime measurements are practically equivalent. The drawback is that in both day and night the lidar signal itself is strongly reduced by extinction due to even small concentrations of ozone in the troposphere. In the past, systems using the latter approach have been described, among others, in [8, 9, 14, 30].

The choice of emitted wavelength is free since Raman scattering is possible at any wavelength, but at the same time it is crucial due to the ozone bands, and in the situation that we have briefly described the availability of a powerful laser source is another crucial parameter that must be considered.

Table 2. System constants considered for lidar system simulations at three Raman wavelengths and two DIAL wavelengths, in combination with the four receiver geometries given in table 1. See text for the meaning of symbols.

λ (nm)	354.7	266	248	724.372	724.348
Type	Raman	Raman	Raman	DIAL	DIAL
Laser source	Nd:YAG THG	Nd:YAG FHG	KrF	dye	dye
λ' (nm)	407.5	294.6	272.7	724.372	724.348
$\Delta\lambda'$ (nm)	0.4	0.3	0.3	2	2
E_0 (mJ)	325	150	200	50	50
f (Hz)	30	30	150	25	25
η_q	25%	25%	25%	5%	5%
η_o	5%	5%	5%	5%	5%
ΔR (m)	150	150	150	150	150
W (Wm^{-2} sr^{-1} nm^{-1})	0.32	4.5×10^{-5}	$< 4 \times 10^{-7}$	0.24	0.24
σ_{on} (m^{-2} sr^{-1})	—	—	—	8.36×10^{-27}	3.12×10^{-27}

We have based our simulation on three different wavelengths, corresponding to available powerful laser sources, in order to evaluate both the 'solar blind' and the 'non-solar blind' approaches (see table 2).

The assumption that is made is that the Raman backscattering cross section does not depend upon temperature. In fact, as explained in [11] the fine structure of the rotational Raman bands is strongly temperature dependent, but the integrated total over the Q-branch is independent since vibrational transitions are negligible at atmospheric temperatures. Therefore, it is the width of the Raman Q-branch that dictates the bandwidth $\Delta\lambda'$ of the receiver to be used. The Raman spectrum of water vapour has been examined in detail in [31], and the part we are interested in is plotted in their figure 3; it shows that the Raman linewidth is approximately 20 cm^{-1} (corresponding to 0.15 nm for the 248 nm emitted wavelength, 0.17 nm for 266 nm and 0.33 nm for 354.7 nm). We have conservatively chosen, for each of the considered wavelengths, a receiver bandwidth ∼0.1 nm larger than this.

4.2. DIAL

DIAL is based on differential absorption at two wavelengths sufficiently close to each other, usually referred to as on-line and off-line. Therefore, the wavelength choice is dictated by the absorption spectrum of water vapour. Several water vapour absorption lines exist in the near-infrared, and especially around 720 and 940 nm. The lines that are mostly used for DIAL applications are around 724 nm, so we have chosen two of these lines for our simulations (see, for instance, [15, 18, 19]). According to [5], these lines are mostly appropriate for moist air conditions as found in the boundary layer at warm marine sites such as Lampedusa, since they are relatively weak, while the longer wavelengths correspond to stronger water vapour lines and are indicated for cold and dry air conditions. As is known from the literature, and we shall also see from the simulations, at one of these wavelengths a really good SNR is obtainable for daytime measurements.

The on-line wavelength λ_{on} that has been considered is 724.372 nm for the first of these lines and 724.348 nm for the second one. Both are in the centre of a 10 pm wide absorption line, the difference being that the first line is much stronger than the second [15]. The off-line wavelength has been conventionally put at $\lambda_{off} = 723.000$ nm and $\sigma_{off} = 0$. These wavelengths can be obtained, for instance, with a tunable dye laser.

Wulfmeyer and Walther [21] illustrate that the selection criterion for water vapour DIAL wavelength is the following: the differential optical depth in a range cell, between the on- and off-line channels, must fall between 0.03 and 0.1. This explains why the wavelength with smaller absorption yields better results with the water vapour concentration that we have considered. In general, as stated in [25], DIAL performance is subject to water vapour content itself, since it may become difficult to detect water vapour in the far range when light is strongly absorbed by large vapour concentrations near to the lidar.

4.3. Common parameters

The four options that we have considered for telescope area and FOV have been given in table 1. The other system constants used in this paper are summarized in table 2. For each wavelength, typical values for E_0, f and η_q for commercially available lasers and photomultipliers have been assumed. For all systems the optical efficiency η_o has been conventionally assumed to be 5% and the range resolution to be 150 m.

The zenith sky spectral radiance at the received wavelength, W, has been derived from measurements of spectral global irradiance taken in 1999 at Lampedusa with a Brewer and a Licor spectrophotometer. To consider a case of largest sky background, the irradiance measurements were taken under clear sky conditions, at noon of the summer solstice (solar zenith angle 12°). In order to estimate the zenith sky radiance, the diffuse irradiance was assumed to be uniformly distributed in a hemisphere, and to derive diffuse irradiance from the global a conventional diffuse-to-direct ratio of 3 has been assumed. Computations with the UVSPEC radiative transfer model [32] have been made to check the validity of this assumption, and they show that the assumed diffuse-to-direct ratio can be considered sufficiently representative in the ultraviolet, i.e. for the Raman channels: values of 1–5 are obtained with different aerosol conditions. At the DIAL wavelengths, an overestimation of the background was probably introduced in our simulations, since the radiative transfer model predicts a larger direct component of solar radiation, with a diffuse-to-direct ratio between 1 and 2.

The atmospheric profiles of $T(0, R)$ and $T'(0, R)$, needed in equation (1), have been derived taking into account

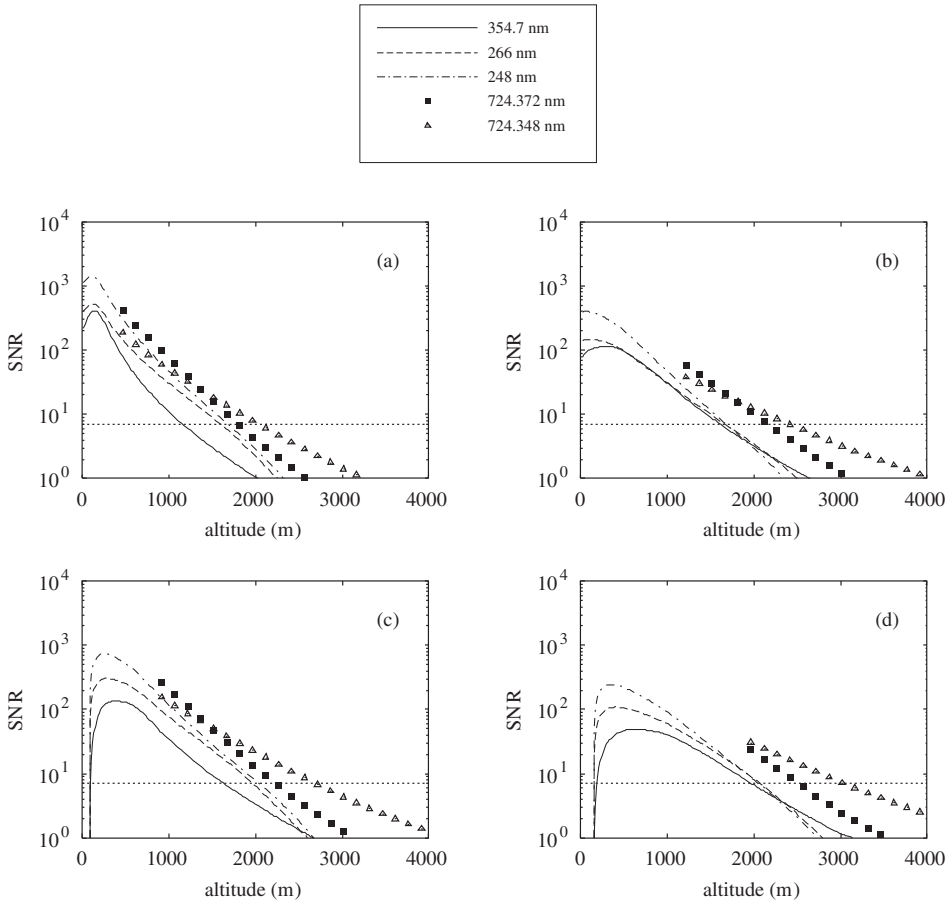

Figure 2. Simulated signal-to-noise ratio (SNR) for 2 min integration time with a Raman lidar operating at 354.7 nm (full curve), 266 nm (broken curve) and 248 nm (chain curve) in daytime. The SNR for a DIAL operated at 724.372 nm (squares) and 724.348 nm (triangles) is also shown. The thin dotted curve denotes the SNR = 7 level assumed to identify the maximum altitude that can be reached. The four plots denote the different receiver geometries listed in table 1: (a) small telescope and large FOV; (b) small telescope and small FOV; (c) large telescope and large FOV: (d) large telescope and small FOV.

extinction due to Rayleigh scattering, aerosols and absorption by ozone (for the UV wavelengths) or water vapour (for the on-line DIAL wavelengths). Rayleigh scattering profiles have been derived from the US Standard Atmosphere [33] by using the well known Rayleigh scattering cross section for the atmosphere (see, e.g., [2]). Aerosol extinction has been conventionally accounted for by assuming a 3 km deep aerosol layer near the ground, having a uniform vertical profile with a total optical depth of 0.75 at 355 nm and an Ångström coefficient of 1.5. Ozone concentration has been conventionally assumed to be 60 ppb by volume, and ozone cross sections were taken from [34]. Water vapour concentration has been derived assuming a 0.005 volume mixing ratio at ground level (equivalent to 30% relative humidity at 15°C) and an exponential decrease with altitude, with a 2.5 km scale height. For DIAL the water vapour absorption cross section has been taken from [15]. Finally, $\beta(R)$ has been calculated taking into account the above-mentioned atmospheric profiles and Rayleigh scattering for DIAL. For Raman lidar, $\beta(R)$ has been deduced by scaling with a λ^{-4} power law the cross section at 248 nm given in [14] (4.1×10^{-33} m^2 sr^{-1} for water vapour and 1.3×10^{-33} m^2 sr^{-1} for nitrogen). Regarding integration time, two cases have been considered: 2 min integration and 30 min integration.

5. Model results

5.1. Simulation of lidar signals

The results of our daytime simulations are plotted in figures 2 and 3 for a 2 min and a 30 min integration time, respectively. For each figure, plots of the SNR for the five system configurations described in table 2 are compared in relation to each of the receiver geometries listed in table 1; for DIAL only range levels with $q(R) = 1$ have been considered. For each system, we consider that the maximum acceptable random error on water vapour concentration is $\sim$15%, corresponding to a SNR of 7. Thus, we denote the maximum height achievable as the one marked by such an SNR. As expected, the systems operating at 248 nm and 266 nm are little influenced by the receiver FOV, since for these systems sky background is negligible.

In all cases, the better performing system for far ranges is DIAL with $\lambda_{on} = 724.348$ nm, despite a relatively low laser power. The other DIAL system ($\lambda_{on} = 724.372$ nm) is much less efficient, due to the higher absorption cross section. Its SNR remains larger than for the Raman lidar case, but it is affected by a larger signal extinction by water vapour itself. A similar reason is the cause of the steep slope in the performance curves of the 248 nm and 266 nm Raman systems,

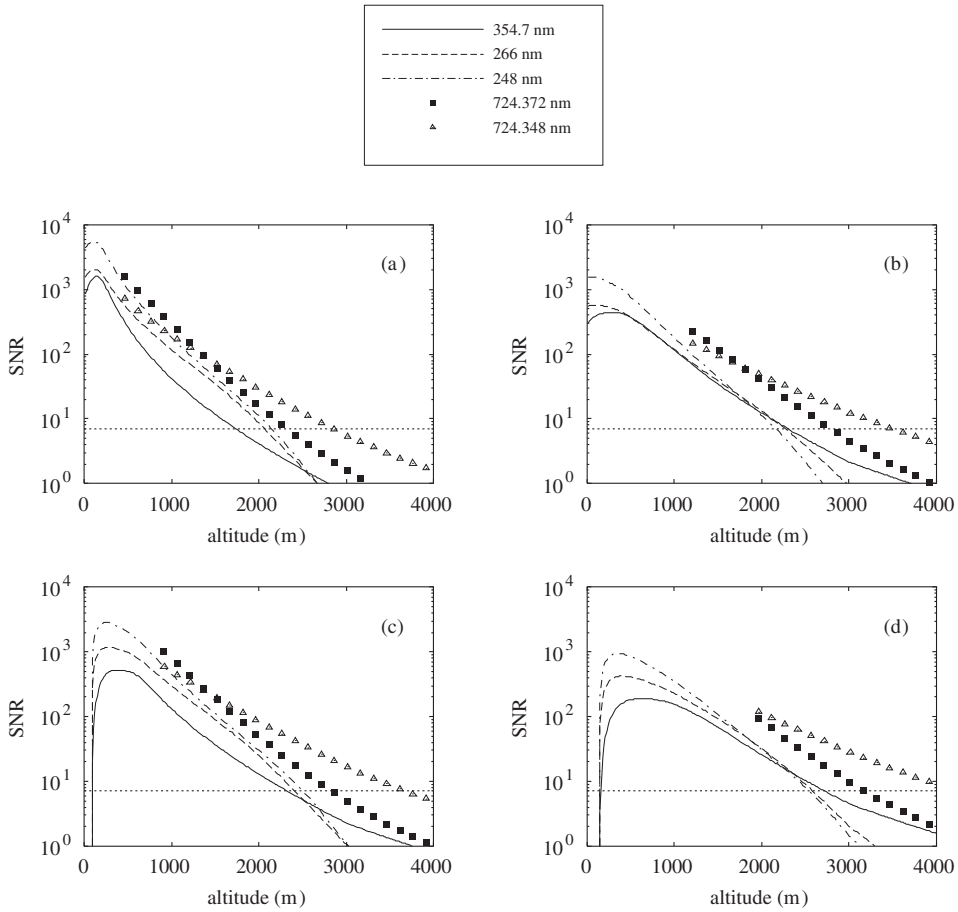

Figure 3. Same as figure 2, but for 30 min integration time.

but extinction this time is due to ozone: these curves begin with high SNR, later cross the 354.7 nm curve and at further ranges they fall below it. Increasing the laser pulse energy or the receiver area by a factor does not help much since signal decay is nearly exponential.

Finally, in the far range the best performing systems among those considered are those operated at a wavelength for which lower atmospheric absorption occurs: 354.7 nm for Raman lidar and 724.348 nm for DIAL. Among the two latter systems, DIAL has the better SNR. Figures 2 and 3 also show how receiver geometry and integration time influence the results. A dual receiver geometry can be an efficient solution for observing a larger range interval.

Since water vapour concentration can be highly variable in both time and space, it is interesting to verify how different humidity profiles affect lidar performance. We have therefore fed into our model different water vapour profiles in use in the scientific community, derived from the US Standard Atmosphere [33], and from the midlatitude summer and winter profiles given in [35]. These humidity profiles are displayed in figure 4(a), where the simple exponential profile used earlier is also shown (open circles); it almost coincides with the midlatitude winter model, the driest of the three cases. Figures 4(b) and (c) display the simulation results for the 354.7 and 724.348 nm wavelengths, respectively, for the case of two different combinations of receiver geometry and integration time. As is obvious, for the Raman case the increase in humidity can only lead to an increase of the SNR and of the maximum achievable range, since the only relevant effect is an increase of the backscattering coefficient. For DIAL, instead, the SNR is slightly improved in the near range only, but signal extinction by water vapour itself reduces performance above $\sim$1 km. The humidity increase from the midlatitude winter profile to the US Standard Atmosphere only slightly affects the SNR curve; however, when humidity is further increased to the midlatitude summer profile, system performance is strongly reduced. Technically, this sort of problem could be overcome by selecting a weaker water vapour absorption line when humidity is large.

5.2. Verification

In order to verify the ability of our calculations to represent a given lidar system, comparison to the results of previous research has been made. Goldsmith and Ferrare [26] describe simulations of a Raman system operating at different wavelengths, and demonstrate that for the 'solar blind' approach the optimum wavelength is around 260 nm, where a range of 4 km should be reached after a 10 min integration, with a SNR $= 10$ level. This result is apparently in disagreement with our computations, which show that it is hard to take measurements further than $\sim$2.5 km at 266 nm with such a SNR. However, their result is based on a very optimistic laser source (500 mJ at 200 Hz), and we are able to reproduce it at

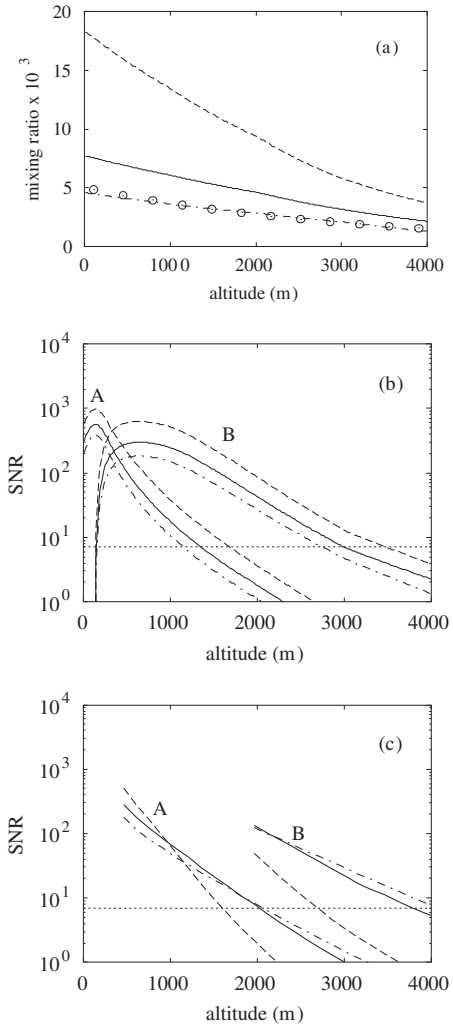

Figure 4. In (a) the water vapour volume mixing ratio profile is displayed according to different models: US Standard Atmosphere, 1976 (full curve); midlatitude summer (broken curve); midlatitude winter (chain curve); exponential decay used in the previous simulations (open circles). The next two plots display the SNR for daytime measurements, computed with different water vapour profiles for (b) Raman lidar at 354.7 nm and (c) DIAL at 724.348 nm: US Standard Atmosphere, 1976 (full curves); midlatitude summer (broken curves); midlatitude winter (chain curves). In each of (b) and (c) two plots are present for each line type, corresponding to two different receiver geometries and averaging times, and are identified by the capital letters placed next to them: A. small telescope, large FOV, 2 min integration; B. large telescope, small FOV, 30 min integration.

266 nm when adapting system parameters to those used in their article, assuming the water vapour profile of the US Standard Atmosphere [33], neglecting the aerosol extinction, assuming a 0.3 mrad FOV, and leaving all other parameters as described in section 4 unchanged.

Another 266 nm computation is presented in [9]: for a 10 Hz 100 mJ laser, slant sounding at 40° elevation, 1.8 nm bandwidth, 2.5 mrad FOV, 35 ppb ozone concentration and 3 min and 20 s integration time (2000 laser shots), a 1.4 km maximum vertical range is predicted. Our model confirms this result. Reference [9] also confirms that the optimum wavelength for 'solar blind' operation is found to be around 266 nm.

Goldsmith and Ferrare [26] present simulation results for the 'non-solar blind' concept based on the 308 nm output wavelength of a XeCl laser, a 0.5 nm filter bandwidth and two different FOVs (0.2 and 2 mrad), obtaining a maximum range of 2.5 and 4 km, respectively, after 10 min integration and with a SNR $= 10$ level. Again, our model is able to predict similar but not identical results (2 and 3.5 km, respectively, or 3 and 4.5 km if we neglect aerosol extinction).

A sophisticated Raman lidar model can be found in [27], where model results are compared to measurements taken at 355 nm with the Department of Energy (DOE) lidar described in [12], and are found to be in agreement. We have fed the system parameters documented in those papers into our computations, have adopted the solar radiance $W = 0.11$ W m^{-2} sr^{-1} nm^{-1} that was found on that particular day, and have assumed a constant water vapour mixing ratio profile corresponding approximately to their experimental data (0.014 by volume; see figure 10 of [27]). According to our results, the lidar system should reach approximately 4 km with a SNR $= 10$ level and with a 1 min temporal resolution; note that the above-mentioned paper displays a profile only going up to 4 km. The approximate SNR calculated from their plot at 2.5 km is 60; our model is slightly more pessimistic since 30 is found. The reader must be warned, though, that this discrepancy is not large when one considers that the curves of SNR versus range fall very steeply (e.g. in our computations the SNR $= 60$ level is found around 2 km instead of 2.5).

Simulation of a 10 W DIAL system operated in the 940 nm region with a 1 m telescope, a 1 nm bandwidth, a narrow 0.2 mrad FOV and large receiver efficiencies (quantum 80% and optical 90%) can be found in [22]. The results of that paper confirm that DIAL is capable of quite extraordinary results, since their simulated system is capable of reaching a vertical range of 9 km with a SNR level of 10 in daytime with a time resolution of 10 min and a range resolution of 300 m. We have compared our simulations with these results and have confirmed the 9 km range by feeding into our model the inputs used in [22].

6. Discussion and conclusions

The lidar model we have described yields results in good agreement with previous work done on the subject for a certain number of wavelengths representative of the spectrum going from the ultraviolet to the near-infrared; when small disagreements are found, the general tendency is for our model to be a little more pessimistic. This reflects the fact that, when faced with doubt or highly variable parameters, we have usually set unfavourable values in the simulation. For instance, optical efficiency is hard to evaluate, and we have therefore conservatively chosen a low value; zenith sky irradiance in the worst case has been used (near noon of the summer solstice), etc. Besides reproducing the results of independent numerical simulations, the model is capable of reasonably reproducing the lidar measurements taken with the DOE Raman lidar, mentioned in [27].

The simulations presented above show that between DIAL and Raman lidar the first yields definitively better results for daytime water vapour profiling. This confirms

the findings presented in the existing literature: see, for instance, [25], where the performance of the DOE Raman lidar is compared with the DIAL system of the Max-Planck-Institut für Meteorologie (MPI). The DOE system is the most powerful existing Raman lidar for water vapour measurements known to us. It is capable of reaching the tropopause at nighttime and ∼3 km in daytime [25], and under certain circumstances it can reach 7 km in daytime [12]. The MPI DIAL, also an extraordinary system, is based on an alexandrite laser and features narrow linewidth, high frequency stability and high purity [25, 36]. The intercomparison showed equivalent performance of the two systems at nighttime, with a 3–5% relative error throughout the PBL. For daytime conditions, while the DIAL maintained a similar accuracy, the Raman system's error rose to 15%.

Among Raman lidars, the computations prove that both 'solar blind' and 'non-solar blind' systems are substantially equivalent and yield a large SNR in the first 1–2 km; however, in the 'solar blind' case the decline of performance with range is steeper, and the 'non-solar blind' case appears more indicated for trying to reach larger distances. As technology evolves, we expect this difference to grow larger, since 'non-solar blind' lidar performance can be improved with a larger laser power, larger receiver efficiency, etc, while in the 'non-solar blind' case the limit is intrinsically given by ozone absorption.

After the above considerations, we remain with two options: one is DIAL at the wavelength of a suitable absorption line (i.e. not a strong line, since otherwise signal extinction would drastically reduce the SNR); the second possibility is the 'non-solar blind' Raman lidar. For daytime measurements, DIAL has certainly a superior performance, since for 'non-solar blind' Raman lidar the large sky background decreases the signal-to-noise ratio. In making a choice, technical difficulties must be accounted for as well, since our system is going to be installed at a remote site, where it is not possible for the operator to make frequent adjustments, and therefore it should be kept as simple as possible. Water vapour absorption lines used for DIAL have a narrow width, of the order of ∼10 pm (this fact is true also for other absorption lines besides those considered here), and even tiny shifts in the laser output wavelength cause large variations of the cross section, which directly enters equation (8). See also [5, 21] on this point: when emitting at the on-line wavelength the laser must have a narrow, stable, and precisely known lineshape. A system that continuously monitors and records variations in σ_{on} is therefore needed (water vapour absorption cell), as well as a feedback control technology for tuning and stabilizing the emitted wavelength. Moreover, the DIAL signal is very sensitive to extinction by water vapour itself, so that the absorption line used should ideally be selected based on atmospheric humidity. The increased experimental complexity makes DIAL more expensive, more difficult to develop and more labour intensive to maintain.

In the end, we have therefore opted for a 'non-solar blind' Raman lidar, based on the 354.7 nm wavelength of the frequency tripled Nd:YAG laser, which permits us to reach a large pulse energy while keeping the system simple to operate. As has been said, at this wavelength the sky background is large in the daytime, and thus narrow receiver bandwidth and FOV are crucial parameters to limit noise. We can verify from the plots in figures 2–4 that with the assumed system parameters we should be able to reach, depending upon the water vapour profile used among those displayed in figure 4(a), the 1.2–1.7 km range with 2 min integration time by using the small telescope with a large FOV (i.e. the most adapted geometry, among those considered, for viewing the nearby layers, with a 'half overlap range' of 150 m). In contrast, to reach far ranges the large telescope with the small field-of-view is best indicated; this geometry is, however, inadequate for making measurements in the first atmospheric layers of the atmosphere (the geometrical form factor is zero up to ∼200 m; it is 0.1 at ∼500 m and 0.5 at ∼900 m). A dual receiver system is therefore needed, using the smaller receiver for the first kilometre, and the larger one for the upper planetary boundary layer. According to our computations, with the large receiver a maximum range of 2–2.6 km can be achieved (depending upon the water vapour profile used) with $\Delta t = 2$ min and with a SNR level of 7; 2.7–3.5 km can be reached with $\Delta t = 30$ min.

Finally, a quantity which should be considered in system design is the photomultiplier count rate. For the considered system and for the assumed ambient radiance level, we calculate for both receivers that the count rate due to the background is approximately 80 MHz. To this, the count rate due to the water vapour signal at the peak must be added, yielding 230 MHz for the small receiver and 100 MHz for the large one with a US Standard Atmosphere [33] humidity profile (the second figure is smaller thanks to the attenuation of the signal in the nearby layers due to the geometrical form factor function). Such large count rates imply either that the detected signal is processed in analogue mode, or that it is attenuated by reducing the optical efficiency, so as to keep below ∼25 MHz and maintain sufficient linearity (after correction for electronic dead time). The reduction of optical efficiency can be achieved, for instance, by using a neutral density filter: this would imply signal attenuation by a factor of 10 for the small receiver and by a factor of 4 for the large one.

The computations have been performed again in this hypothesis, in order to verify how system performance would be affected with the small telescope–large FOV geometry and with the large telescope–small FOV geometry. The reduction of the maximum measurable range, according to the SNR = 7 criterion, has been calculated for the different water vapour profiles shown in figure 4(a). This reduction is ∼0.4 km in all cases, except that it tends to be a little larger (∼0.5 km) for the moister water vapour profile (mid-latitude summer). Although significant, the reduction is not excessive, thanks to the fact that both the signal and the background are equally reduced by a neutral density filter. Besides the possibility of reducing the optical efficiency, another possibility is to reduce the telescope area (by keeping the same FOV). Both things are equivalent for what concerns SNR above the overlap range, as shown from equation (5); however, the two cases differ in the geometrical form factor function, and the smaller receiver may yield a larger signal peak. The use of two small telescopes (or one small telescope with a dual FOV option) is therefore another efficient possibility, provided that the signal intensity at this larger peak is checked in order not to exceed the desired count rate.

The ability to reach far ranges for different lidars can be compared by calculating the figure-of-merit given in equation (5). We compare this quantity for the 354.7 nm

system summarized in table 2 and for the DOE system [12]. The two systems differ mainly in the following technological constants (when the artificially introduced attenuation is not considered): E_0, A, θ and $\Delta\lambda'$. When only the variation in these four quantities is considered, we find that the DOE lidar's figure-of-merit is larger by a factor of 2.8 with respect to our simulated system with the large telescope–small FOV geometry. This performance gap can be compensated when a degradation of the range and time resolutions is introduced: for the DOE system, these are, respectively, 39 m and 1 min, while in our computations we have assumed a 150 m vertical resolution. It can be seen that, when $\Delta t = 2$ min for our system, both systems should achieve an identical $K_L/\sqrt{N_0}$ ratio when exposed to similar ambient conditions (i.e. the same W). Since the DOE system is probably the most powerful water vapour Raman lidar to date, and it has been found to reach 7 km in daytime in some cases [12], we might expect a similar performance in certain circumstances (smaller ambient radiance when the sun is at a larger solar zenith angle, smaller aerosol load, etc.). However, degrading the resolution may represent a limitation to the type of science that can be made with the measured water vapour profiles.

Acknowledgments

Thanks to Vincenzo Santacesaria for providing his computer code for geometrical form factor calculations, and to Daniela Meloni for providing radiative transfer computations for the evaluation of the solar vertical radiance. Thanks also to the anonymous reviewers of this paper for their valuable advice.

References

[1] Westwater E R 1997 Remote sensing of tropospheric temperature and water vapor by integrated observing systems *Bull. Am. Meteorol. Soc.* **78** 1991–2006

[2] Hinkley E D (ed) 1976 *Laser Monitoring of the Atmosphere* (Berlin: Springer)

[3] Ansmann A, Neuber R, Rairoux P and Wandinger U (eds) 1997 *Advances in Atmospheric Remote Sensing with Lidar* (Berlin: Springer)

[4] Dabas A, Loth C and Pelon J (eds) 2001 *Advances in Laser Remote Sensing* (Palaiseau, France: Éditions de l'École Polytechnique)

[5] Grant W B 1991 Differential absorption and Raman lidar for water vapor profile measurements: a review *Opt. Eng.* **30** 40–8

[6] Melfi S, Lawrence J and McCormick M 1969 Observations of Raman scattering by water vapor in the atmosphere *Appl. Phys. Lett.* **15** 295–7

[7] Cooney J A 1970 Remote sensing measurements of atmospheric water vapour profiles using the Raman component of laser backscatter *J. Appl. Meteorol.* **9** 182–4

[8] Renaut D, Pourny J C and Capitini R 1980 Daytime Raman-lidar measurements of water vapor *Opt. Lett.* **5** 233–5

[9] Renaut D and Capitini R 1988 Boundary-layer water vapor probing with a solar-blind Raman lidar: Validations, meteorological observations and prospects *J. Atmos. Ocean. Technol.* **5** 585–601

[10] Vaughan G, Wareing D P, Thomas L and Mitev V 1988 Humidity measurements in the free troposphere using Raman backscatter *Quart. J. Roy. Meteor. Soc.* **114** 1471–84

[11] Whiteman D N, Melfi S H and Ferrare R A 1992 Raman lidar system for the measurement of water vapor and aerosols in the Earth's atmosphere *Appl. Opt.* **31** 3068–82

[12] Goldsmith J E M, Blair F H, Bisson S E and Turner D D 1998 Turn-key Raman lidar for profiling atmospheric water vapor, clouds, and aerosols *Appl. Opt.* **37** 4979–90

[13] Bisson S E, Goldsmith E and Mitchel M G 1999 Narrow-band, narrow field-of-view Raman lidar with combined day and night capability for tropospheric water-vapor profile measurements *Appl. Opt.* **38** 1841–9

[14] De Tomasi F, Perrone M R, Protopapa M L and Torsello G 2000 Ground-based Raman lidar for day and night measurements of water-vapor in the boundary layer *Nuovo Cimento* **C23** 587–96

[15] Browell E V, Wilkerson T D and McIlrath T J 1979 Water vapor differential absorption lidar development and evaluation *Appl. Opt.* **18** 3474–83

[16] Browell E V 1983 Remote sensing of tropospheric gases and aerosols with an airborne DIAL system *Optical and Laser Remote Sensing* ed K D Killinger and A Mooradian (Berlin: Springer) pp 138–47

[17] Senff C, Bösenberg J and Peters G 1994 Measurement of water vapor flux profiles in the convective boundary layer with lidar and radar-RASS *J. Atmos. Ocean. Technol.* **11** 85–93

[18] Kiemle C, Ehret G, Giez A, Davis K J, Lenschow D H and Oncley S P 1997 Estimation of boundary layer humidity fluxes and statistics from airborne differential absorption lidar (DIAL) *J. Geophys. Res.* **102** 29 189–203

[19] Giez A, Ehret G, Schwiesow R L, Davis K J and Lenschow D H 1999 Water vapor flux measurements from ground-based vertically pointed water vapor differential absorption and Doppler lidars *J. Atmos. Ocean. Technol.* **16** 237–50

[20] Wulfmeyer V 1999 Investigation of turbulent processes in the lower troposphere with water vapor DIAL and radar-RASS *J. Atmos. Sci.* **56** 1055–76

[21] Wulfmeyer V and Walther C 2001 Future performance of ground-based and airborne water-vapor differential absorption lidar: I. Overview and theory *Appl. Opt.* **40** 5304–20

[22] Wulfmeyer V and Walther C 2001 Future performance of ground-based and airborne water-vapor differential absorption lidar: II. Simulations of the precision of a near-infrared, high-power system *Appl. Opt.* **40** 5321–36

[23] Chamard P, Ciattaglia L, Monteleone F and di Sarra A 1999 The station for climate observations at Lampedusa: greenhouse gas measurements *Proc. the X CO_2 Expert Meeting* (World Meteorological Organization) at press

[24] di Sarra A *et al* 2001 Radiation, ozone and aerosol measurements at Lampedusa during the PAUR-II campaign *IRS2000: Current Problems in Atmospheric Radiation* (Hampton, VA: Deepak) pp 1193–6

[25] Linné H, Turner D D, Goldsmith J E M, Tooman T, Bösenberg J, Ertel K and Lehman S 2001 Intercomparison of DIAL and Raman lidar measurements of humidity profiles *Advances in Laser Remote Sensing* ed A Dabas, C Loth and J Pelon (Palaiseau, France: Éditions de l'École Polytechnique)

[26] Goldsmith J E M and Ferrare R A 1992 Performance modeling of daytime Raman lidar systems for profiling atmospheric water vapor *Proceedings of the Sixteenth International Laser Radar Conference* ed M P McCormick (NASA Conference Publication **3158**), 667–70

[27] Whiteman D N, Schwemmer G, Berkoff T, Plotkin H, Ramos-Izquierdo L and Pappalardo G 2001 Performance modeling of an airborne Raman water-vapor lidar *Appl. Opt.* **40** 375–90

[28] Halldorsson T and Langerholc J 1978 Geometrical form factors for the LIDAR function *Appl. Opt.* **17** 240–4

[29] Santacesaria V, Marenco F, Balis D, Papayannis A and Zerefos C 1998 Lidar observations of the Planetary Boundary Layer above the city of Thessaloniki, Greece *Nuovo Cimento* **21** 585–96

[30] Petri K, Salik A and Cooney J 1982 Variable-wavelength solar-blind Raman lidar for remote measurements of atmospheric water-vapor concentration and temperature *Appl. Opt.* **21** 1212–18
[31] Avila G, Fernández J M, Maté B, Tejeda G and Montero S 1999 Ro-vibrational Raman cross sections of water vapor in the OH stretching region *J. Mol. Spec.* **196** 77–92
[32] Mayer B, Seckmeyer G and Killing A 1997 Systematic long-term comparison of spectral UV measurements and UVSPEC modeling results *J. Geophys. Res.* **102** 8755–67
[33] US Standard Atmosphere 1976 (Washington, DC: NOAA, NASA, US Air Force)
[34] Molina L T and Molina M J 1986 Absolute cross-sections of ozone in the 185-to-350 nm wavelength range *J. Geophys. Res.* **91** 14 501–8
[35] Anderson G P, Clough S A, Kneizys F X, Chetwynd J H and Shettle E P 1986 AFGL Atmospheric Constituent Profiles (0-120 km) (Hascom Air Force Base, MA: AFGL-TR-86-0110, Air Force Geophys. Lab.)
[36] Wulfmeyer V and Bösenberg J 1998 Ground-based differential absorption lidar for water vapor profiling: Assessment of accuracy, resolution, and meteorological applications *Appl. Opt.* **37** 3825–44